Materials Advances

ROYAL SOCIETY OF CHEMISTRY

PAPER

View Article Online
View Journal | View Issue

Cite this: *Mater. Adv.*, 2024, 5, 9851

White light emission and superior color stability in a single-component host with exceptional eminent color rendering and theoretical calculations on D_{uv} for color quality†

Wasim Ullah Khan,[ab] Waheed Ullah Khan,[c] Haris Zaman,[d] Ayaz Mahsud,[e] Dilfaraz Khan,*[e] Salim Ullah Khan,[f] Shuakat Khan[g] and Yueli Zhang *[ab]

Received 18th September 2024,
Accepted 11th November 2024

DOI: 10.1039/d4ma00937a

rsc.li/materials-advances

Correlated color temperature (CCT) is widely used to describe the chromaticity of white light sources, although chromaticity is only two-dimensional, and the distance from the Planckian locus is typically absent. Herein, a novel single-phase $Ca_3YAl_3B_4O_{15}$:Tm^{3+},Dy^{3+},Eu^{3+}, an emerging white-emitting phosphor with good optical properties and thermal-stability, is produced, and the practical calculation methods to calculate the chromaticity-shift (ΔE) and D_{uv} value for color-quality are also demonstrated, making it a good contender for possible use in LEDs. The incorporation of Eu^{3+} into $Ca_3YAl_3B_4O_{15}$:0.015Tm^{3+},0.08Dy^{3+} resulted in attractive warm-white light with CCT declining from 4635 K to 3065 K. The $Ca_3YAl_3B_4O_{15}$:Tm^{3+},Dy^{3+},Eu^{3+} exhibited excellent thermal stability (I@400 K = ~93%). The $Ca_3YAl_3B_4O_{15}$:Tm^{3+},Dy^{3+},Eu^{3+}-based WLED exhibits satisfactory parameters of high R_a (89.9) and low-CCT (3065 K). Additionally, this article offers useful mathematical strategies for calculating D_{uv} over a wide-range of chromaticity, from 2000 to 6000 K in CCT and from −0.002 to 0.014, which strongly matches the range in an American National Standards Institute (ANSI) standard. For the first time, white light with minimized thermal-quenching, improved CRI, and color quality has been used in near-UV chip-excited WLEDs.

1. Introduction

One of the most important characteristics of light sources for general illumination is chromaticity, which is typically defined using CIE coordinates (x, y) or (u, v). But these two numbers don't convey the color information.[1,2] The chromaticity information of general light sources is frequently provided *via* correlated color temperature (CCT) for practical applications. However, CCT only offers one dimension of chromaticity; the other dimension is the position of chromaticity concerning the Planckian locus and is typically absent. Some areas of the industry have been using the term "D_{uv}" (Deviation of Uniform Visual perception) or concepts akin to it, such as the distance from the Planckian locus for this purpose, although these terms have not been formally defined in any standards. An American National Standards Institute standard recently defined D_{uv}.[3] White LEDs, which are anticipated to be the next-generation light source,[4,5] have gained popularity as a hot topic in lighting applications.[6–9] YAG:Ce^{3+} and InGaN-based blue chips are usually used to create commercially available WLEDs. RBG light emission could be obtained by either single-phase or multi-color phosphors.[6,10–12] The serious flaw in these systems is that they fall short of ideal standards. The challenge of producing white light in a single-component host has generated a significant deal of attention due to the substantial reabsorption of blue light by green and red. By adding a red phosphor to the system, warm white light with a high R_a is produced, producing the desired qualities.[13] Meanwhile, the single-component phosphors play a vital role compared with the multi-phase photoluminescence materials, offering a higher color-rending index (CRI), better stability, better reproducibility, low manufacturing costs, no phase separation, and an informal fabrication method.[14–16] Fortunately, it is possible to introduce a

[a] *Analysis and testing center, Shenzhen Technology University, Shenzhen, 518118, P. R. China*
[b] *School of Materials Science and Engineering, Sun Yat-sen University, Guangzhou 510275, P. R. China. E-mail: stszyl@mail.sysu.edu.cn*
[c] *School of New Materials and New Energies, Shenzhen Technology University, Shenzhen, 518060, P. R. China*
[d] *Institute of Chemical Sciences, Peshawar University, Peshawar, Khyber Pakhtunkhwa, 29050, Pakistan*
[e] *Institute of Chemical Sciences, Gomal University, Dera Ismail Khan, Khyber Pakhtunkhwa, 29050, Pakistan. E-mail: dilfarazkhan@gu.edu.pk*
[f] *Department of Chemistry, University of Science and Technology Bannu, Khyber Pakhtunkhwa, 29050, Pakistan*
[g] *Department of Chemical Engineering, College of Engineering, Dhofar University, Salalah 211, Sultanate of Oman*

† Electronic supplementary information (ESI) available. See DOI: https://doi.org/10.1039/d4ma00937a

sensitizer to enhance the activator's emission, as was done previously.[14,15] Consequently, using energy transfer (ET) to produce white light is still a hot topic.[17]

Of all the rare-earth ions, Dy^{3+} seems to be a noble candidate for white emission in hosts with a single phase. Dy^{3+} activated phosphors have been the subject of practical investigations because it is simple to produce white emission by altering the proportion of blue and yellow emissions from Dy^{3+}, which correspond to the transitions of $^4F_{5/2} \rightarrow {}^6H_{15/2}$ and $^4F_{5/2} \rightarrow {}^6H_{13/2}$.[18,19] However, the Dy^{3+}-activated phosphors exhibit a significant CCT issue that prevents their use in more vibrant applications.[20]

As mentioned above, they do not meet the prime desires of WLEDs. They still have the drawbacks of a low CRI and cold white light with a CCT $>$ 6000 K because there is no red light in the spectrum, which prevents them from being used in applications that require more vibrant colors.[9,21–24] Implementing more emissions in the red spectral regions is vital to resolving these issues and enhancing luminous performances. These can be effectively resolved by co-doping Tm^{3+} and Dy^{3+} into a host and another red-emitting center. Trivalent Eu^{3+} can produce red light originating from its ground state of $^7F_0$ to excited states (*e.g.* $^5D_4 \sim 362$ nm, $^5L_8 \sim 366$ nm, $^5G_4 \sim 375$ nm, $5G_2 \sim 380$ nm, and $^5L_6 \sim 393$ nm). It can be an effective activator for presentations and unquestionably is a fantastic choice when used as a red-component center for WLEDs.[25,26] It is possible to compensate for the emission of phosphors in the red area and increase the optical performance by co-doping Tm^{3+}–Dy^{3+} and Eu^{3+}. Consequently, multiple techniques need to be employed to broaden the emission of co-doped phosphors containing Tm^{3+}, Dy^{3+}, and Eu^{3+}. The structure of $Ca_3YAl_3B_4O_{15}$ belongs to the space group $P63/m$, which is isostructural to gaudefroyite $Ca_4(MnO)_3(BO_3)_3CO_3$. There are two available sites (Ca1 & Ca2) for the substitution of dopant ions. These sites are separated by BO_3 and AlO_6 groups, and yttrium ions occupy the Ca1 site.[27,28]

This work presents the development of a single-component $Ca_3YAl_3B_4O_{15}$:Tm^{3+},Dy^{3+},Eu^{3+} warm white phosphor with exceptional optical properties. XRD, crystal-refinements, TEM, DRS, and detailed optical properties characterized the resulting samples, and D_{uv} is suggested as a simple way to express the chromaticity of white light sources for general illumination, together with color stability or chromaticity-shift (ΔE). Quantitative analysis was done on the crystal structure and the impact of Dy^{3+} doping on the electrical structure of CYAB, which has a prominent effect. Interestingly, the incorporation of Eu^{3+} into $Ca_3YAl_3B_4O_{15}$:$0.015Tm^{3+}$,$0.08Dy^{3+}$ displayed attractive warm-white-light with CCT declining from 4635 K to 3065 K. Furthermore, a WLED device with a CRI of 89.9% was achieved by Eu^{3+} codoping. Additionally, this article provides useful calculation techniques for calculating D_{uv} over a wide range of chromaticity, from −0.002 to 0.014 in D_{uv} and 2000 to 6000 K in CCT.

2. Experimental section

2.1 Sample preparation

All reagents were obtained in pure form from commercial sources and were used directly. H_3BO_3 (A.R.), Y_2O_3, Eu_2O_3, Tm_2O_3, $CaCO_3$ (A.R.), $Al(OH)_3$ (A.R.), and Dy_2O_3 were sourced from Aladdin. The reagents were carefully combined in a stoichiometric ratio and crushed. After being placed in the crucible, the mixture was heated there for 10 hours at 900 °C. Then, for a further ten hours, it was heated at 1100 °C in a CO-reduction environment. The obtained phosphors are as follows; $Ca_3Y_{1-x}Al_3B_4O_{15}$:xEu^{3+} (x = 0.1, 0.3, 0.5, 0.8,), $Ca_3Y_{1-x}Al_3B_4O_{15}$:xTm (x = 0.005, 0.01, 0.015, 0.02, 0.025), $Ca_3Y_{1-x}Al_3B_4O_{15}$:xDy (x = 0.01, 0.04, 0.08, 0.12, 0.16), and $Ca_3Y_{0.985-x}Al_3B_4O_{15}$:$0.015Tm^{3+}$,$0.08Dy^{3+}$,$xEu^{3+}$ (x = 0.00, 0.001, 0.007, 0.01, 0.02). The produced phosphors were then employed for additional characterization (see the ESI† for more information).

3. Results and discussion

3.1 Structural characterization, micromorphology, and DFT calculations

Powder X-ray diffraction patterns of $Ca_3YAl_3B_4O_{15}$:xDy^{3+} (x = 0.01 to 0.16) samples are presented in Fig. 1a. The JCPDS dataset was used to index the prepared phosphor diffraction peaks (172 154). The X-ray diffraction study results showed that doping of Dy^{3+} does not have any other impurities or cause any notable change. As shown in Fig. S1 (ESI†), the Rietveld-refinement results of $Ca_3YAl_3B_4O_{15}$:Dy^{3+} confirmed that the phosphor crystalizes into a single garnet phase. The cell variables were a = 10.3867(3), c = 5.8146(2), and V = 534.94 Å^3. The unit cell contains four distinct types of cationic sites, where the metal ions exhibit nine-fold and seven-fold coordination polyhedra at the $Ca^{2+}/Y^{3+}(1)$ and $Ca^{2+}/Y^{3+}(2)$ sites, respectively. Additionally, six coordinated aluminum sites and three coordinated boron sites were discovered. The $Ca^{2+}/Y^{3+}(1)$ sites were separated from the $Ca^{2+}/Y^{3+}(2)$ sites by the BO_3 and AlO_6 units in Fig. 1b and c. The AlO_6 octahedra share edges to form chains, which are connected by triangular BO_3 groups in the ab plane, creating a Kagome-type lattice characteristic of the gaudefroyite structure. The $P63/m$ space group accurately predicts all points in the X-ray diffraction pattern. However, the Ln^{3+} rare-earth ions in $Ca_3YAl_3B_4O_{15}$ have somewhat different distributions in these two sites, as Ln^{3+} ions can occupy both cation sites in the structure, with the $Ca^{2+}/Y^{3+}(1)$ sites being occupied by 79% Ln^{3+} ions and the $Ca^{2+}/Y^{3+}(2)$ sites being occupied by 21% Ln^{3+}.[29] As for our system, the dopant's behavior is opposite to what has been previously reported.[30] Our modifications showed that the $Ca^{2+}/Y^{3+}(2)$ site in $Ca_3YAl_3B_4O_{15}$:Dy^{3+} should be occupied by a very heavy-ion, rather than the $Ca^{2+}/Y^{3+}(1)$ site. Thus, we assume that in $Ca_3YAl_3B_4O_{15}$:Dy^{3+} ions fully occupy the $Ca^{2+}/Y^{3+}(2)$ site. As shown in Fig. 1c (coordinating conditions of $Ca^{2+}/Y^{3+}(1)$ and $Ca^{2+}/Y^{3+}(2)$), the distance between the sites of $Ca^{2+}/Y^{3+}(1)$ is shorter than the $Ca^{2+}/Y^{3+}(2)$ sites, which may be the reason for the preferences of occupancy (Table S1, ESI†). All the other elements containing Ca, Y, Dy, Al, and O in the matrix were detected except boron (Fig. 1d and e). The (1 1 2) and (−1 2 1) planes are well represented by a lattice fringe in the HRTEM picture with interplanar lattice spacings of 0.52 and 0.35 nm of $Ca_3YAl_3B_4O_{15}$:$0.08Dy^{3+}$ shown in Fig. S2 (ESI†). The XPS results gave

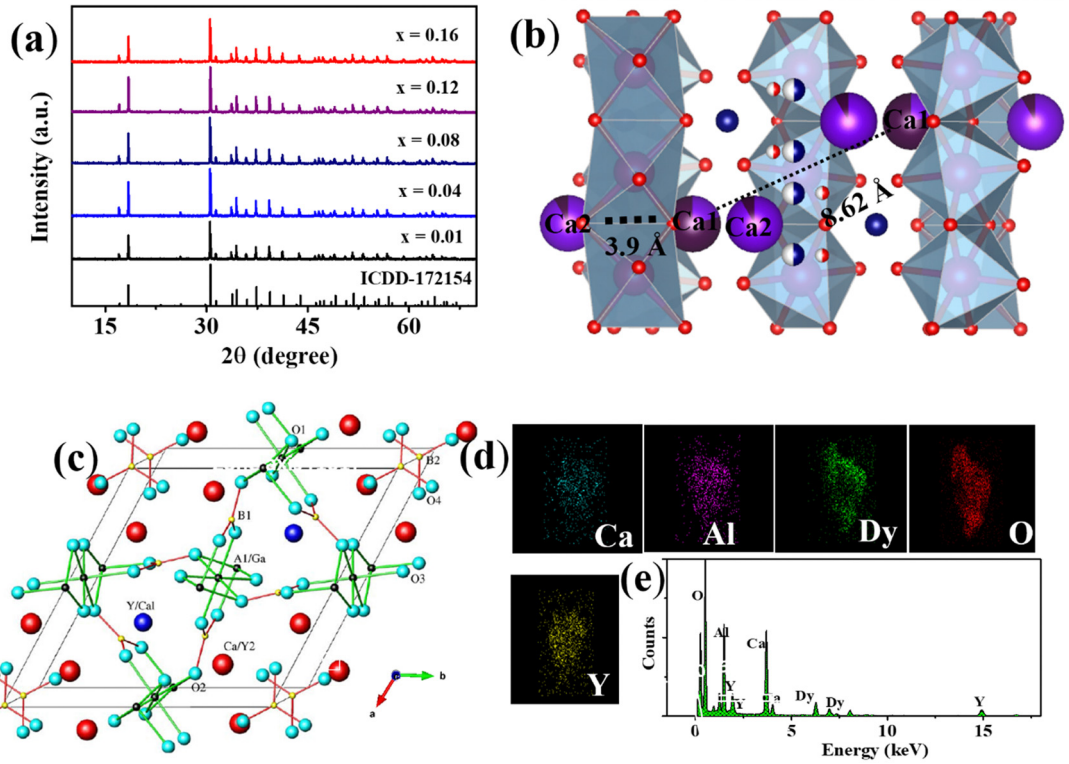

Fig. 1 (a) XRD pattern of $Ca_3YAl_3B_4O_{15}$:xDy^{3+} (y = 0.01 to 0.16). (b) and (c) coordination environments of CYAB and (d) and (e) EDS elemental distribution.

additional proof for the elemental makeup (Fig. 2). XPS spectral analysis showed peaks at 284.5 eV and 530.7 eV attributed to C 1s and O 1s, respectively (details are given in the ESI†).[31] The Kubelka–Munk function was used to calculate the phosphors' energy bandgap (E_g), which was found to be 5.13 eV from the diffuse reflection spectroscopy (DRS) analysis (Fig. 3a and b).[32]

3.2 Photoluminescence properties of Tm^{3+}/Dy^{3+}/Eu^{3+} single doped $Ca_3YAl_3B_4O_{15}$

Fig. 4a and b show the PLE and PL spectra of $Ca_3YAl_3B_4O_{15}$:Eu^{3+}. The wide band between 250 and 300 nm, peaking at about 265 nm, and numerous brilliant, crisp lines between 300 and 480 nm are present in the PLE spectra recorded at 618 nm. The CTB transition from the filled 2p orbitals of O^{2+} ions to the partially filled 4f orbitals of Eu^{3+} was first thought to be responsible for the broadband emission (Fig. 4a).[14] $Ca_3YAl_3B_4O_{15}$:xEu^{3+} phosphors were found to emit strong red light at 394 nm excitation. The PL spectra of $Ca_3YAl_3B_4O_{15}$:xEu^{3+} (x = 0.1, 0.3, 0.5, 0.8) phosphors with various Eu^{3+} doping concentrations are shown in Fig. 4b under excitation at 397 nm. Each sample showed typical red Eu^{3+} ion emissions, and the intensity of the $^5D_0 \rightarrow {}^7F_2$ emission was altered. There was no concentration quenching effect seen when the doping level increased as suggested by the concentration-dependent luminescence intensity of $Ca_3YAl_3B_4O_{15}$:Eu^{3+}. The $Ca_3YAl_3B_4O_{15}$:Eu^{3+} sample's CIE coordinates were found to be (0.653, 0.342), which was relatively near to the NTSC standard value for red phosphor (0.670, 0.330). Notably, the CIE value of $Ca_3YAl_3B_4O_{15}$:Eu^{3+} was superior to that of the commercial phosphor Y_2O_2S:Eu^{3+} (0.622, 0.351), as shown in Fig. S3a (ESI†).[33] Color purity is regarded as a crucial component of a material's efficiency for WLED applications. The following equation was used to obtain the color purity for all the samples that were doped with Eu^{3+}.[33–35]

$$\text{Color purity} = \frac{\sqrt{(x-x_i)^2+(y-y_i)^2}}{\sqrt{(x_d-x_i)^2+(y_d-y_i)^2}} \times 100\% \quad (1)$$

where (x, y), (x_i, y_i), and (x_d, y_d) correspond to the CIE diagrams of the phosphor, white illumination, and dominant wavelength. $Ca_3YAl_3B_4O_{15}$:xEu^{3+} was found to have a color purity of 93.8% in Fig. S3a (ESI†), which exceeds the value of the previously known red-emitting phosphors.[23,36–43] The decay curves of $Ca_3YAl_3B_4O_{15}$:xEu^{3+} are explored in Fig. S3b (ESI†). Eqn (2) provides a good match to the appropriate results for all of the analyses.[33–35]

$$I = B\exp(-t/\tau) \quad (2)$$

where I refers to the photoluminescence intensity at time t, B is a constant, and τ is the luminescence lifetime, respectively. The value of τ is adjusted to 1.22 ms so that the second-order exponential may more easily fit decay curves. For a deeper look at the luminescence performance, we assessed the IQE of the $Ca_3YAl_3B_4O_{15}$:Eu^{3+} sample. Under 394 nm excitation, the IQE of $Ca_3YAl_3B_4O_{15}$:xEu^{3+} reached 82.5%, which is higher than that of the commercial phosphor Y_2O_2S xEu^{3+} (IQE: 35%).[33]

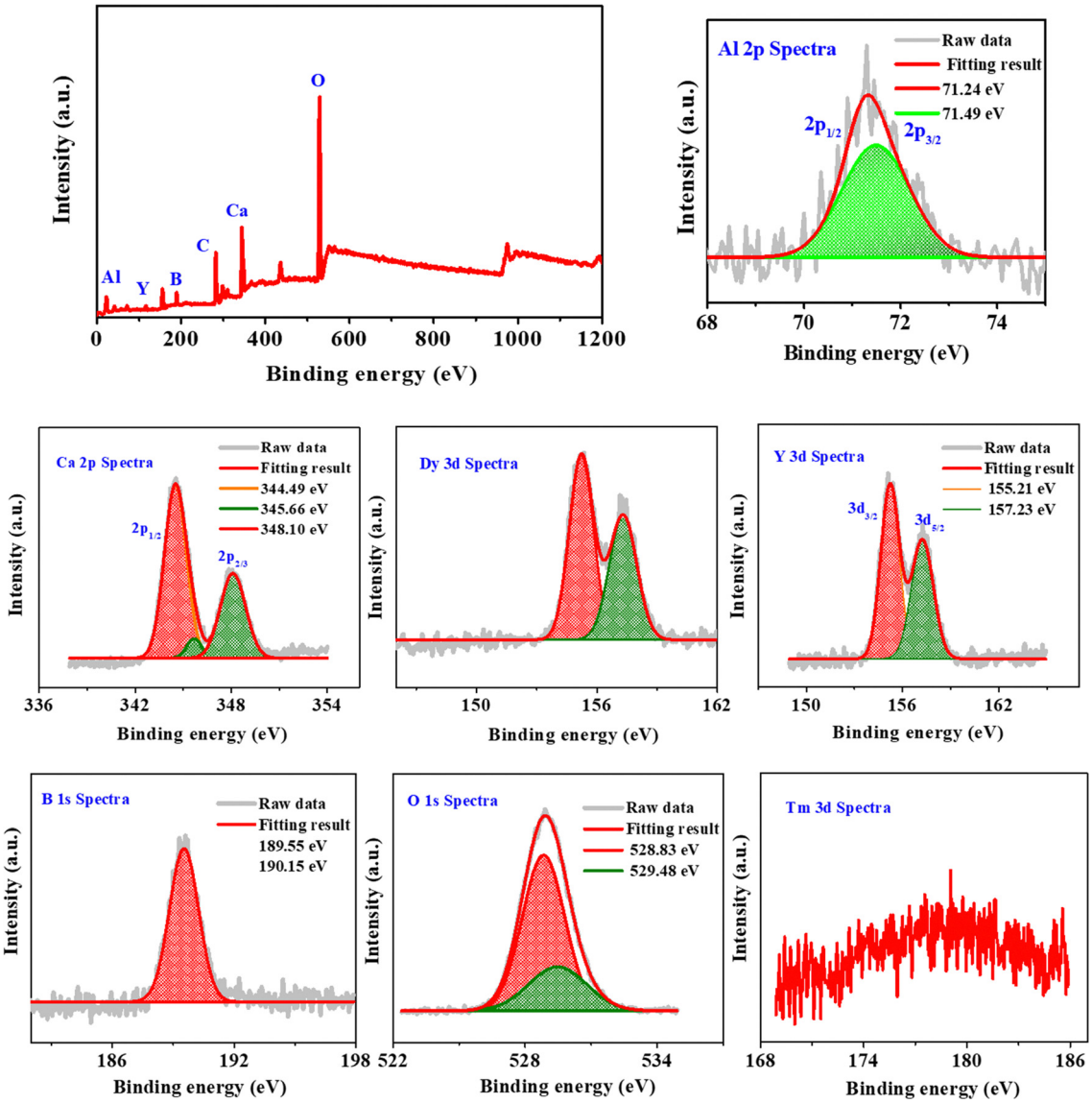

Fig. 2 XPS spectra of CYAB:Tm^{3+},Dy^{3+} and XPS spectral analysis of Al, Ca, Dy, Y, B, O, and Tm.

Thermal stability is a highly significant parameter that can affect the phosphor's color output and brightness. Consequently, Fig. S3c (ESI†) displays the temperature-dependent spectra of $Ca_3YAl_3B_4O_{15}$:xEu^{3+}. Unexpectedly, the PL intensity at 400 K was around 85.2% higher than at 303 K. This shows that the $Ca_3YAl_3B_4O_{15}$:xEu^{3+} phosphor has better heat stability and is suitable for making WLEDs. After that, the activation energy (E) was determined using the Arrhenius equation and the thermal quenching data are shown in Fig. S3d (ESI†). In contrast to the literature, the heat stability of phosphors is typically significantly healthier (Table 1).

The excitation and emission spectra of $Ca_3YAl_3B_4O_{15}$:Tm^{3+} and concentration-dependent photoluminescence intensity of the $Ca_3Y_{1-x}Al_3B_4O_{15}$:xTm^{3+} (x = 0.005–0.025) phosphor are presented in Fig. 4c and d. The PLE achieved by placing the detector at 456 nm contains a sharp absorption band at 358 nm attributed to the $^3H_6 \rightarrow {}^1D_2$ transition of Tm^{3+}. The phosphor emits characteristic light associated with $^1D_2 \rightarrow {}^3F_4$ transitions of Tm^{3+} peaking at 456 nm, under 360 nm excitation. The $Ca_3Y_{1-x}Al_3B_4O_{15}$:xTm^{3+} emission spectrum displayed an increase in emission intensity under stimulation at 356 nm. The quenching concentration of $Ca_3Y_{1-x}Al_3B_4O_{15}$:xTm^{3+} is depicted in Fig. 4d. The cross-relaxation between $^1D_2$ and $^3F_4$ energy levels is what causes quenching. The energy level's schematic picture shows how the transition of Tm^{3+} in CYAB is likely to occur. The chromaticity diagram of $Ca_3YAl_3B_4O_{15}$:Tm^{3+} was obtained using the PL spectrum in Fig. S5a (ESI†), and it was found to be (0.154, 0.042), which was extremely near to the BAM:Eu^{2+} blue light (0.170, 0.045). The temperature-dependent PL spectra of $Ca_3YAl_3B_4O_{15}$:Tm^{3+} from 300 K to 500 K are displayed in Fig. S4b (ESI†). Unexpectedly, the PL intensity at 400 K was approximately 91% higher than at 303 K. This shows that the $Ca_3YAl_3B_4O_{15}$:Tm^{3+} phosphor has better heat stability and is suitable for making WLEDs. After that, the activation energy was determined using the

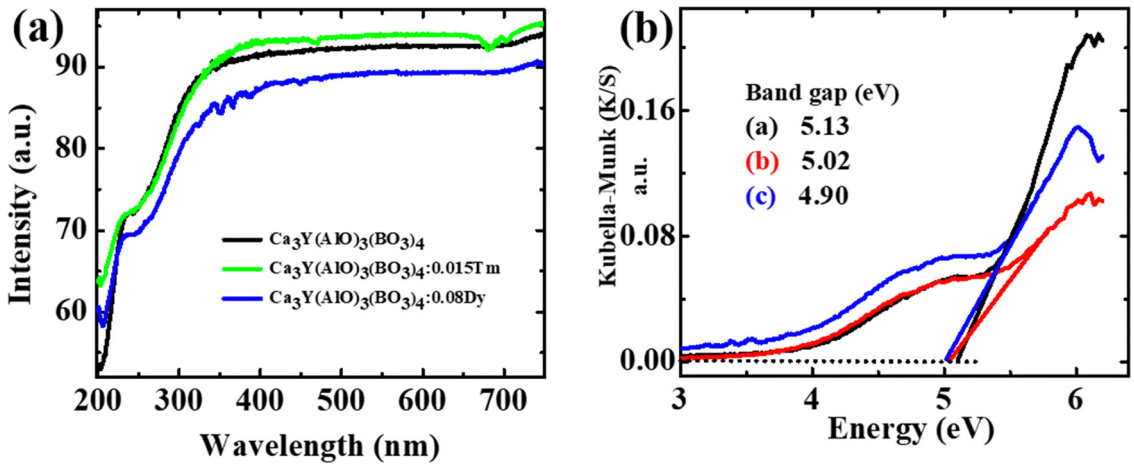

Fig. 3 (a) and (b) DR spectra, and the bandgap DRS spectra of the CYAB, CYAB:0.015Tm^{3+} CYAB:0.08Dy^{3+} phosphors.

Arrhenius equation and the thermal quenching data in Fig. S4c (details are given in the ESI†). The thermal stability of $Ca_3YAl_3B_4O_{15}$:Eu^{3+} phosphor is superior to that reported in the literature (Table 1).

Besides, the PLE and PL spectra of the Dy^{3+}-activated $Ca_3YAl_3B_4O_{15}$ are illustrated in Fig. S5a and b (ESI†). The excitation spectrum was obtained by placing a detector at 570 nm ($^4F_{9/2} \rightarrow {}^6H_{13/2}$). The f–f transitions of Dy^{3+} are responsible for several peaks in the excitation. A series of peaks observed at 295, 324, 340, 351, 365, 389, 426, 452, and 475 nm match the $^6H_{15/2}$ to $\Delta J = 2$ transition.[55] The $Ca_3Y_{1-x}Al_3B_4O_{15}$:xDy^{3+} emission spectrum under 350 nm excitation (y = 0.01, 0.04, 0.08, 0.12, and 0.16) showed increasing emission intensity (Fig. S5b, ESI†). The magnetic dipole ($^4F_{9/2} \rightarrow {}^6H_{15/2}$) transition of Dy^{3+} is thought to be responsible for the emission peaks at 474 and 489 nm, which seldom change with the chemical environment or the crystal field nearby Dy^{3+}. Another key emission peak at 569 nm is from the $^4F_{9/2} \rightarrow {}^6H_{13/2}$ (electric dipole) transition. Dy^{3+} ions undergo the forced electric dipole transition *via* a $^4F_{9/2} \rightarrow {}^6H_{13/2}$ hypersensitive transition ($\Delta J = 2$), which is largely controlled by the chemical atmosphere close to the Dy^{3+}. Fig. S5c (ESI†) demonstrates the temperature-dependent PL spectra of $Ca_3YAl_3B_4O_{15}$:Dy^{3+} from 300 K to 500 K. It is evident that when the temperature increased, the PL of Dy^{3+} decreased. The emission intensities dropped until they reached 89.6% at 400 K (Fig. S5d, ESI†). The primary aspect governing the potential usage of phosphor is the temperature-dependent properties of materials. The decay curves for Dy^{3+} in CYAB at various doping concentrations (x = 0.01, 0.04, 0.08, 0.12, and 0.16) are presented in Fig. S6a (ESI†). By adjusting the value of τ to be between 0.38 and 0.26 ms, the first-order exponential (eqn (2)) may suit decay curves effectively, as shown in Fig. S6a (ESI†).

The critical distance (RC) between Dy^{3+} ions must be determined to study the CQ process, and it was determined that the RC value was 9.98 Å (ESI†). Therefore, in the CQ process of the Dy^{3+} ion, the multipolar–multipolar interaction dominated. The following equation was utilized to comprehend the link

Table 1 Assessment of the recent and earlier literature based on thermal stability, correlated color temperature (CCT), color rendering (R_a), color stability or chromaticity shift (ΔE) and D_{uv} value for color stability

	Materials	Thermal stability	CCT	R_a	D_{uv}	ΔE	Ref.
1	$K_2BaCa(PO_4)_2$:Eu^{2+}	96%	5326	85.0	None	None	44
2	(Sr,Ca)$AlSiN_3$:Eu^{2+}	78%	6119	92.2	None	None	45
3	$SrLiAl_3N_4$:Eu^{2+}	81%	3738	85.0	None	None	46
4	$NaBiF_4$:Eu^{3+}	67%	6851	88.2	None	None	23
5	$Ca_3YAl_3B_4O_{15}$:Eu^{3+}	85.2%	None	None	None	None	This work
6	$Ca_3YAl_3B_4O_{15}$:Tm^{3+}	91.3%	None	None	None	None	This work
7	$Ca_3YAl_3B_4O_{15}$:Dy^{3+}	89.5%	None	None	None	None	This work
8	$CaSc_2O_4$:0.15Eu^{3+},0.03Sm^{3+}	96.1%	5348	81.0	None	None	47
9	$Na_2Y_2Ti_3O_{10}$:Eu^{3+},Sm^{3+}	84%	5556	83.0	None	None	48
10	Cs_2NaYCl_6:Sb^{3+},Mn^{2+}	None	5410	81.2	None	None	49
11	$Rb_{0.5}K_{1.5}Ca_{0.995}PO_4$(F, Cl):$Eu^{2+}$	87%	4163	93.3	None	None	50
12	Sn^{2+}/Mn^{2+} glass	56%	3811	95.3	None	None	9
13	SLGO:Dy^{3+},Sm^{3+}	50%	5284	91.1	None	None	26
14	$Ba_3GdNa(PO_4)_3F$ Eu^{2+}	~60%	5402	81.0	None	None	51
15	$Zn(SCN)_2$	None	6046	86.0	None	None	52
16	$CsPbX_3$	None	8335	93.0	None	None	53
17	$Cs_2AgInCl_6$	None	3878	85.0	None	None	54
18	$Ca_3YAl_3B_4O_{15}$:Tm^{3+},Dy^{3+} Eu^3	93%	3065	89.9	−0.006	12.31×10^{-3}	This work

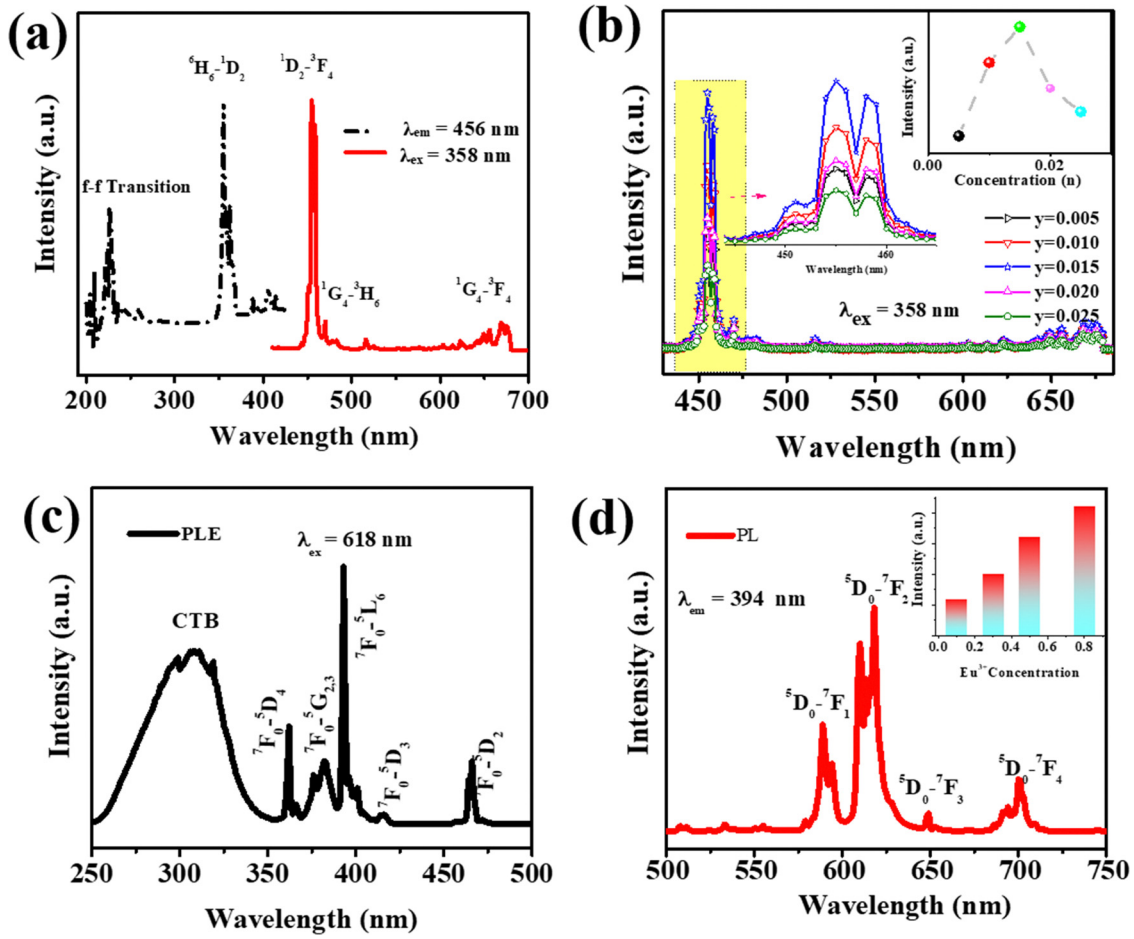

Fig. 4 (a) PLE and PL spectra, and (b) concentration-dependent luminescence intensity of the $Ca_3YAl_3B_4O_{15}$:xTm^{3+}. (c) PLE and (d) PL spectra (with the inset showing the concentration-dependent luminescence intensity) of the $Ca_3YAl_3B_4O_{15}$:xEu^{3+}.

between PL intensity (I) and Dy^{3+} concentration (x);[33–35]

$$\log\frac{I}{x} = \log\left[1 + \beta(x)^{S/3}\right]^{-1} \quad (3)$$

where S stands for multipolar interaction and β is a constant. When a similar activator is doped, CQ causes EM to occur as depicted in Fig. S6b (ESI†). And s = 6, 8, and 10 correspond to the interactions between D–D (dipole–dipole), D–Q (dipole–quadrupole), and Q–Q (quadrupole–quadrupole), respectively. As a result, S = 6.27, which is closer to 6 showing that in $Ca_3YAl_3B_4O_{15}$:Dy^{3+}, the electric D–D mechanism predominates.

3.3. Single-component white light emission

The CIE coordinates of Tm^{3+} and Dy^{3+}-activated $Ca_3YAl_3B_4O_{15}$ were observed to be (0.160, 0.062) and (0.358, 0.386) respectively, matching the colors of blue and yellow, for the co-doped phosphors and were based on their corresponding emission spectra as (0.321, 0.335) and (0.338, 0.364) for the $Ca_3YAl_3B_4O_{15}$:0.015Tm^{3+},0.08Dy^{3+} phosphor. Under excitation at 358 nm, the $Ca_3YAl_3B_4O_{15}$:0.015Tm^{3+},0.08Dy^{3+} phosphor displayed strong white light emissions that were simply tuned from blue (Tm^{3+}) to yellow (Dy^{3+}). The CIE coordinates of the phosphor (0.321, 0.335) are very close to those of daylight (0.333, 0.333), corresponding to a color temperature of 5742 K. Furthermore, it is important to highlight that warm white light with a correlated color temperature (CCT) below 5000 K is particularly desirable in solid-state lighting applications. Therefore, Eu^{3+} ions are used in the $Ca_3YAl_3B_4O_{15}$:0.015Tm^{3+},0.08Dy^{3+},xEu^{3+} phosphor to enhance the red-emission. The presence of ET between Tm^{3+} and Eu^{3+} ions is suggested by the fact that the excitation bands of Eu^{3+} and Tm^{3+} overlap to some degree in the 450–465 nm region (Fig. S7, ESI†). The emission spectra of $Ca_3Y_{0.905-x}Al_3B_4O_{15}$:0.015$Tm^{3+}$, 0.08$Dy^{3+}$,$xEu^{3+}$ (x = 0.001, 0.007, 0.01, 0.02) phosphors (λ_{ex} = 358 nm, λ_{ex} = 361 nm) are given in Fig. 5a and b. The CIE diagram of $Ca_3Y_{0.905-x}Al_3B_4O_{15}$:0.015$Tm^{3+}$,0.08$Dy^{3+}$,$xEu^{3+}$ is shown in Fig. 5c and d and the data are given in Table S2 (ESI†). By appropriately adjusting the dopant concentration of Tm^{3+}, Dy^{3+}, and Eu^{3+}, it is possible to realize nearly the entire white light area upon excitation of 361 nm. The synthesized $Ca_3YAl_3B_4O_{15}$:0.015-Tm^{3+},0.08Dy^{3+},xEu^{3+} (x = 0.007, 0.01, 0.02) phosphors exhibited exceptionally alluring warm-white-light emissions with CCT of 4635 K, 3406 K, and 3065 K as given in the insets of Fig. 5. Because 358 nm light is not highly efficient for excitation of Eu^{3+}, additional Eu^{3+} ions are required to generate warm white-light emission. At the same time, a minor amount of Eu^{3+} is sufficient for a 361 nm excitation. The $Ca_3YAl_3B_4O_{15}$:0.015Tm^{3+},0.08Dy^{3+},xEu^{3+}

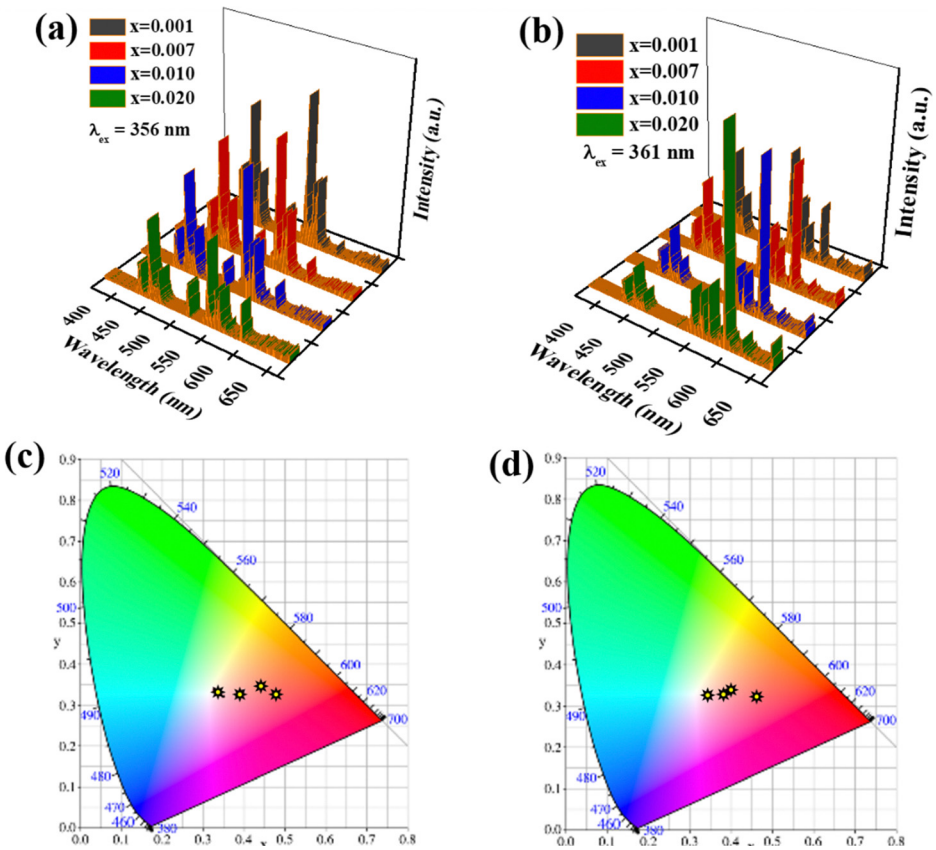

Fig. 5 (a) and (b) Photoluminescence properties and (c) and (d) CIE diagram of CYAB:0.015Tm^{3+},0.08Dy^{3+},xEu^{3+} with (λ_{ex} = 358 nm, λ_{ex} = 361 nm) excitation.

phosphor luminescence decay times are depicted in Fig. S7 and Table S3 (ESI†). It is evident from Fig. S7 (ESI†) that raising the Eu^{3+} concentration reduces the decay durations for Tm^{3+} ions. Furthermore, to evaluate the ET phenomenon from Tm^{3+} into the activator, the decay plots of the sensitizer Eu^{3+} in CYAB:Tm^{3+},Dy^{3+} were considered. The mechanism often relies on dipole–dipole or dipole–quadrupole interactions, where energy can transfer effectively from one dopant ion to another based on the Dexter ET model described elsewhere.[24,25] As presented in Fig. S7b (ESI†), the best linear relationship was detected when n = 6 for the lifetime (τ/τ_0) *versus* the $x^{n/3}$, where x is the concentration of the sensitizer and activator. The rate of ET and ET efficiency were calculated using the equation $k_{ET} = 1/\tau - 1/\tau_0$, and $\eta = 100(1 - \tau/\tau_0)$, where τ and τ_0 define the Tm^{3+} sensitizer lifetime with and without an activator. The calculated value of k_{ET} rate and ET efficiency (η) as a function of Eu^{3+} concentration in $Ca_3YAl_3B_4O_{15}$:0.015Tm^{3+},0.08Dy^{3+},xEu^{3+} were as high as 97.58 μs^{-1} and 72.92%, as seen in Fig. S7b and Table S3 (ESI†). The Tm^{3+} ions will probably sensitize the Eu^{3+} emissions. The phosphors with ET adjustment are obviously more appropriate for WLEDs.

3.4 Thermal and color stability in a single-component host

Thermal stability is a critical factor affecting the performance of white light-emitting diodes (WLEDs), particularly in maintaining their efficiency and longevity under operational conditions. Typical operating temperatures for WLEDs range from 50 °C to 100 °C, influenced by factors such as power levels, heat dissipation design, and environmental conditions. Lower-power WLEDs generally operate at around 50–70 °C, while high-power variants can reach 80–100 °C or higher, especially in demanding environments. Thermal stability plays a crucial role in maintaining WLED performance under these conditions, as materials with high thermal stability help mitigate thermal quenching, ensuring consistent brightness and color accuracy. This stability prolongs device lifespan and improves energy efficiency by allowing more electrical energy to be converted into visible light rather than being lost as heat. Therefore, thermally stable phosphors and LEDs are essential for applications ranging from residential lighting to industrial and outdoor settings.[6,56] Fig. 6a shows the emission spectra of $Ca_3YAl_3B_4O_{15}$:0.015Tm^{3+},0.08Dy^{3+},0.02Eu^{3+} at varying temperatures from 300 K to 550 K at 361 nm. The steady loss of emission intensity was primarily attributed to the increased non-radiative emission at higher temperatures. The inset in Fig. 6b displays the integrated variation trend of the emission intensity of the $Ca_3YAl_3B_4O_{15}$:0.015Tm^{3+},0.08Dy^{3+},0.02Eu^{3+} sample at different temperatures. The total luminescence at 400 K was found to preserve 93% of its level at ambient temperature. Even at 475 K, the light intensity was maintained at 83.34% of room temperature, demonstrating the phosphor's high thermal stability. It is important to note that the thermal stability of the Eu^{3+} emission in the tridoped system was greatly

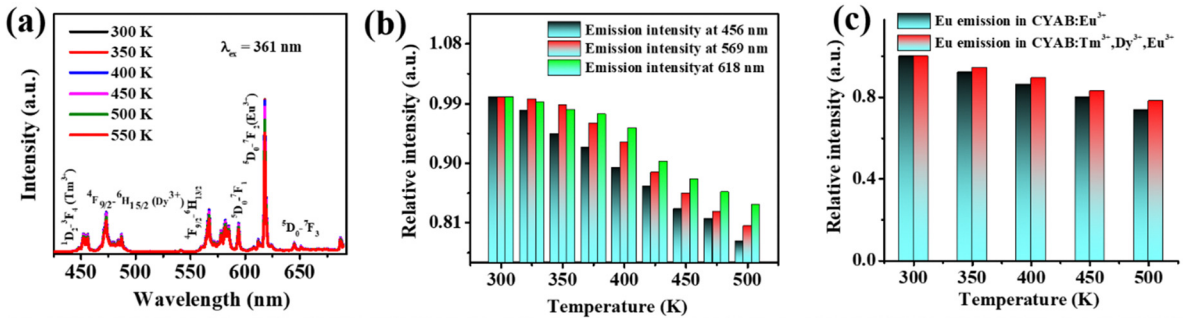

Fig. 6 (a) The temperature-dependent PL spectra of $Ca_3YAl_3B_4O_{15}$:0.015Tm^{3+},0.08Dy^{3+},0.02Eu^{3+} and (b) Tm^{3+}, Dy^{3+} and Eu^{3+} emission intensities that are dependent on temperature as a function of temperature and (c) comparison with the PL intensity of a singly doped Eu^{3+} activator.

improved when compared to the single-doped examples, whereas the thermal stability of the Tm^{3+} luminescence continues to decline. According to Fig. 6c, there appears to be a "temperature enhancement effect" that balances the thermal quenching of Eu^{3+} and Dy^{3+} and enhances Eu^{3+} emission. High color stability can finally be realized. The color stability can be quantitatively explained by the chromaticity shift (ΔE) using the following equation.[6]

$$\Delta E = \sqrt{(u_t' - u_0')^2 + (v_t' - v_t')^2 + (w_t' - w_0')^2} \quad (5)$$

where $u' = 4x/(3 - 2x + 12y)$, $v' = 9y/(3 - 2x + 12y)$, and $w' = 1 - u' - v'$. x and y are the chromaticity coordinates. The chromaticity shift values are listed in Table S4 (ESI†). At 400 K, the conventional white light-emitting phosphor chromaticity shift is around 7.61×10^{-3}. It is notable that at 400 K, the value of ΔE_s is 7.61×10^{-3}, which is significantly lower than that of industrial phosphors, such as $BaMgAl_{10}O_{17}$ with ΔE_s of 15.2×10^{-3}, and $CaAlSiN^{3+}$ with ΔE_s of 44×10^{-3}. This demonstrates that the studied phosphor shows strong resistance to color shift, which is essential for reliable performance in mini and micro-LED applications.

3.5. Application to white LEDs and D_{uv} color quality of light sources for lighting

In practical applications, thermally stable phosphors play a crucial role in enhancing energy efficiency, lowering maintenance costs, and ensuring a reliable and consistent light source. This stability is particularly important in settings where color accuracy and stable light output are essential, such as in commercial displays, healthcare environments, and residential lighting, where sustained color fidelity is desired. WLEDs that are environmentally friendly, exhibit high luminance, and possess a long lifespan are valuable across various applications. The single-phase white emission and good thermal stability make the $Ca_3YAl_3B_4O_{15}$:0.015Tm^{3+},0.08Dy^{3+},0.02Eu^{3+} phosphor an attractive candidate for solid-state lighting. The construction of the LED lamp involved utilizing a 360 nm UV LED chip, along with the $Ca_3YAl_3B4O_{15}$:0.015Tm^{3+},0.08Dy^{3+},0.02Eu^{3+} emitting sample, to showcase the vivid application of the synthesized phosphor (Fig. 7a). The electroluminescence spectrum displayed numerous emission peaks at about 455, 473, 573, 613, 650, and 700 nm, which originated from the phosphor shown in Fig. 7b. Most importantly, the corresponding R_a value up to 89.9 was better than that of other stated phosphors, as listed in Table 1. These findings identified

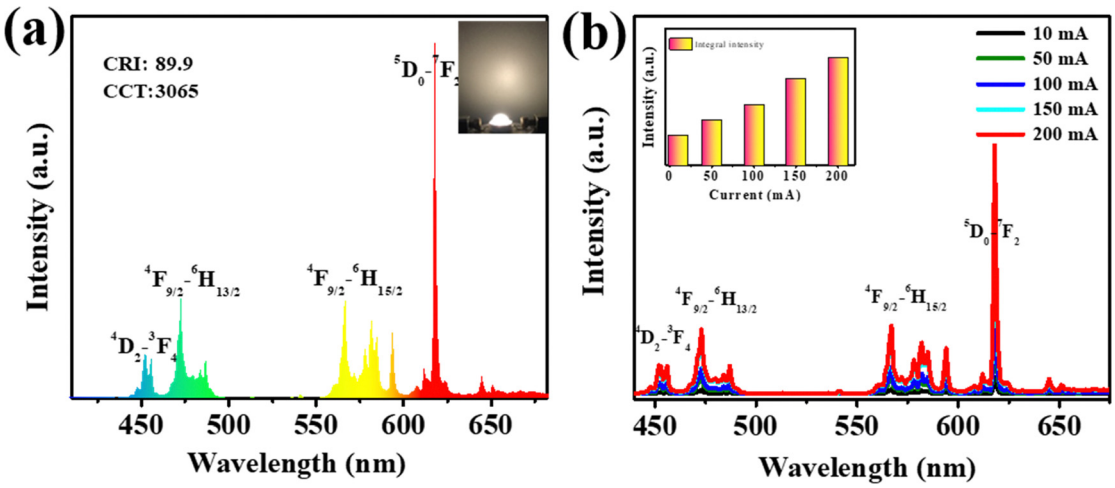

Fig. 7 (a) WLED device fabricated using the optimized $Ca_3YAl_3B_4O_{15}$:0.015Tm^{3+},0.08Dy^{3+},0.02Eu^{3+}. (b) EL spectra of the WLED derived by the different currents.

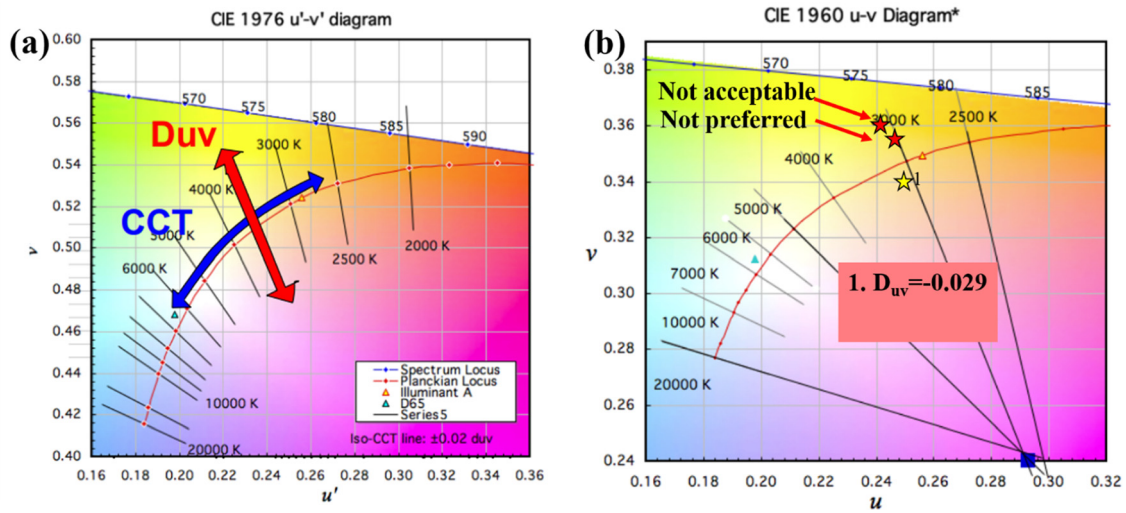

Fig. 8 (a) and (b) CCT-D_{uv} chart based on the CIE 1976 (u, v) diagram and CCT-D_{uv} chart of $Ca_3YAl_3B_4O_{15}$:0.015Tm^{3+},0.08Dy^{3+},0.02Eu^{3+} on the CIE 1976 diagram.

that $Ca_3YAl_3B_4O_{15}$:0.015Tm^{3+},0.08Dy^{3+},0.01Eu^{3+} is appropriate for generating intense white emission upon UV light excitation.

When talking about color-sensitive lighting applications, the D_{uv} (D_{uv}) computation is a crucial measure.[1,2] D_{uv} is crucial for the color accuracy of light sources. D_{uv} is frequently overlooked in specifications. When describing the chromaticity of white light sources, correlated color temperature (CCT) is frequently utilized. However, as chromaticity is only two-dimensional, the distance from the Planckian locus is frequently absent. Though not yet extensively used, D_{uv} is specified in ANSI C78.377 for this purpose. This is because CCT and CRI do not fully explain color quality. D_{uv} explains how far the light coordinate point is from the blackbody curve. The chromaticity of light sources can be specified using CCT and D_{uv} exactly like (x, y). Contrary to (x, y), the two integers (CCT, & D_{uv}) intuitively provide color information. CIE must specify what D_{uv} is. The formula below converts the CIE 1931 x and y values to their equivalent D_{uv} values.[3]

(1) Convert (x, y) or (u', v') to (u, v)

$$u = 4x/(-2x + 12y + 3) \quad u = u'$$

$$v = 6y/(-2x + 12y + 3) \text{ or } v = 2v'/3$$

(2) D_{uv} is obtained by

$$L_{FP} = \sqrt{(u - 0.292)^2 + (v - 0.24)^2}$$

$$a = \arccos\left(\frac{u - 0.292}{L_{FP}}\right)$$

$$L_{BB} = k_6a^6 + k_5a^5 + k_4a^4 + k_3a^3 + k_2a^2 + k_1a + k_0$$

$$D_{uv} = L_{FP} - L_{BB}$$

where, $k_0 = -0.471106$, $k_1 = 1.925865$, $k_2 = -2.4243787$, $k_3 = 1.5317403$, $k_4 = -0.5179722$, $k_5 = -0.08939440$, and $k_6 = -0.00616793$. The equation above can easily be used to compute D_{uv}. The calculated value of D_{uv} of the typical white emission is about −0.002 to 0.014 (Fig. 8 and Table 1). Using the above equation, the calculated value of D_{uv} for $Ca_3Y_{0.985-x}Al_3B_4O_{15}$:0.015$Tm^{3+}$,0.08$Dy^{3+}$,$x$$Eu^{3+}$ is listed in Table S4 (ESI†). The recommended D_{uv} range is −0.006 to +0.006 according to ANSI and Energy Star. A D_{uv} range between −0.003 and +0.003 is ideal for practical uses that are more demanding (Waveform Lighting's FilmGrade series of products have a D_{uv} tolerance of ±0.003). The computed value of D_{uv} in this study is between −0.002 to +0.014, which strongly matches the range in the ANSI standard.[3] The term D_{uv} represents the deviation from the blackbody locus on a chromaticity diagram, indicating the color difference between the light source and natural daylight or blackbody radiation at a similar CCT. In lighting, D_{uv} is critical because even small deviations can mark the perception of warmth, neutrality, or coolness, making it a key parameter in human-centric lighting applications.

4. Conclusion

Novel $Ca_3YAl_3B_4O_{15}$ phosphors with Tm^{3+}, Dy^{3+}, and Eu^{3+} doping were studied to determine their possible applications, chromaticity shift, or color stability, and D_{uv} is recommended as a simple way to understand the chromaticity of white light sources used for general lighting. The $Ca_3YAl_3B_4O_{15}$:Tm^{3+}, $Ca_3YAl_3B_4O_{15}$:Dy^{3+}, and $Ca_3YAl_3B_4O_{15}$:Eu^{3+} samples exhibited the characteristic transitions of Tm^{3+} ($^3H_6 \rightarrow {}^1D_2$), Dy^{3+} ($^6H_{15/2} \rightarrow J_{3,17,5,13}$), and Eu^{3+} ($^5D_{0,1,2} \rightarrow {}^7F_{0,1,2,3,4}$). The incorporation of Eu^{3+} into $Ca_3YAl_3B_4O_{15}$:0.015Tm^{3+},0.08Dy^{3+} displayed attractive warm-white light with CCT declining from 4635 K to 3065 K. Importantly, the temperature-dependent PL of $Ca_3YAl_3B_4O_{15}$:0.015Tm^{3+},0.08Dy^{3+},0.02Eu^{3+} at 400 K was 93% of that at 300 K, showing excellent thermal stability. With the incorporation of Eu^{3+} as a coactivator into $Ca_3YAl_3B_4O_{15}$:0.015Tm^{3+},0.08-Dy^{3+},$x$$Eu^{3+}$ (x = 0.007, 0.01, and 0.02), the CIE coordinates can

be adjusted from (0.3279, 0.3259) to (0.4559, 0.3376), with CCT dropping from 4535 K to 3065 K. The $Ca_3YAl_3B_4O_{15}$:Tm^{3+},-Dy^{3+},Eu^{3+}-based WLED exhibits satisfactory parameters of high R_a (89.9) and low-CCT (3065 K). Furthermore, this article provides useful calculation techniques for calculating D_{uv} over a wide range of chromaticity, from −0.002 to 0.014 in D_{uv} and 2000 to 6000 K in CCT. The computed value of D_{uv} is ±0.002 to ±0.014, which strongly matches the range in an American National Standards Institute (ANSI) standard.

Data availability

Data will be made available on request. The datasets supporting this article have been uploaded as part of the ESI.†

Conflicts of interest

The authors declare that they have no conflicts of interest.

Acknowledgements

This work was supported by the National Natural Science Foundation of Guangdong Province (2414050004479), and the Science and Technology Planning Project of Shenzhen Municipality under grant no. 20241063010062. The Chinese Scholarship Council, China postdoc, and the Guangdong Government are acknowledged for the support to Dr Wasim Ullah Khan during their PhD and postdoc fellowship.

References

1 D. Baxter, M. Royer and K. Smet, *Leukos*, 2024, **20**, 55–66.
2 M. Royer, M. J. Murdoch, K. Smet, L. Whitehead, A. David, K. Houser, T. Esposito, J. Livingston and Y. Ohno, *Leukos*, 2023, **19**, 35–52.
3 B. Das, S. Bardhan, T. Maity and S. Mazumdar, *Results Optics*, 2020, **1**, 100013.
4 P. Pust, V. Weiler, C. Hecht, A. Tücks, A. S. Wochnik, A.-K. Henß, D. Wiechert, C. Scheu, P. J. Schmidt and W. Schnick, *Nat. Mater.*, 2014, **13**, 891.
5 A. Layek, P. C. Stanish, V. Chirmanov and P. V. Radovanovic, *Chem. Mater.*, 2015, **27**, 1021–1030.
6 J. Li, Q. Liang, J.-Y. Hong, J. Yan, L. Dolgov, Y. Meng, Y. Xu, J. Shi and M. Wu, *ACS Appl. Mater. Interfaces*, 2018, **10**, 18066–18072.
7 S. Liang, L. Song, W. Nie, Z. Wang, D. Chen, F. Lin and H. Zhu, *Adv. Opt. Mater.*, 2024, **12**, 2301502.
8 W. U. Khan, L. Qin, W. U. Khan, S. U. Khan, M. M. Hussain, F. Ahmed, S. Kamal and P. Zhou, *ACS Appl. Nano Mater.*, 2023, **6**, 17838–17847.
9 Y. Zhang, B. Chen, X. Zhang, Y. Cao, J. Zhang, S. Xu, X. Li, H. Yu, D. Gao, X. Sha, L. Wang, X. Chen and H. Lin, *Chem. Eng. J.*, 2023, **467**, 143467.
10 Y. Wei, L. Cao, L. Lv, G. Li, J. Hao, J. Gao, C. Su, C. C. Lin, H. S. Jang and P. Dang, *Chem. Mater.*, 2018, **30**, 2389–2399.
11 P. Zhu, Q. Zhu, H. Zhu, H. Zhao, B. Chen, Y. Zhang, X. Wang and W. Di, *Opt. Mater.*, 2008, **30**, 930–934.
12 W. U. Khan, L. Qin, A. Alam, P. Zhou, Y. Peng and Y. Wang, *Nanoscale*, 2021, **13**, 4301–4307.
13 D. Wen, J. Shi, M. Wu and Q. Su, *ACS Appl. Mater. Interfaces*, 2014, **6**, 10792–10801.
14 W. U. Khan, J. Li, X. Li, Q. Wu, J. Yan, Y. Xu, F. Xie, J. Shi and M. Wu, *Dalton Trans.*, 2017, **46**, 1885–1891.
15 W. U. Khan, L. Zhou, Q. Liang, X. Li, J. Yan, N. U. Rahman, L. Dolgov, S. U. Khan, J. Shi and M. Wu, *J. Mater. Chem. C*, 2018, **6**, 7612–7618.
16 W. U. Khan, L. Qin, P. Zhou, A. Alam, Z. Ge and Y. Wang, *ACS Appl. Mater. Interfaces*, 2023, **15**, 45616–45625.
17 F. Jahanbazi, N. Dimakis and Y. Mao, *Adv. Opt. Mater.*, 2024, **12**, 2301219.
18 T. Nakajima and T. Tsuchiya, *ACS Appl. Mater. Interfaces*, 2015, **7**, 21398–21407.
19 J. Long, F. Chu, Y. Wang, C. Zhao, W. Dong, X. Yuan, C. Ma, Z. Wen, R. Ma and M. Du, *Inorg. Chem.*, 2017, **56**, 10381–10386.
20 Y. Liu, G. Liu, J. Wang, X. Dong and W. Yu, *Inorg. Chem.*, 2014, **53**, 11457–11466.
21 J. Qiao, L. Ning, M. S. Molokeev, Y.-C. Chuang, Q. Liu and Z. Xia, *J. Am. Chem. Soc.*, 2018, **140**, 9730–9736.
22 Z. Wang, J. Ha, Y. H. Kim, W. B. Im, J. McKittrick and S. P. Ong, *Joule*, 2018, **2**, 914–926.
23 P. Du, X. Huang and J. S. Yu, *Chem. Eng. J.*, 2018, **337**, 91–100.
24 W. U. Khan, P. Zhou, L. Qin, A. Alam, Z. Ge and Y. Wang, *Mater. Today Nano*, 2022, **18**, 100205.
25 R. Shi, J. Xu, G. Liu, X. Zhang, W. Zhou, F. Pan, Y. Huang, Y. Tao and H. Liang, *J. Phys. Chem. C*, 2016, **120**, 4529–4537.
26 Z. Zhang, J. Li, N. Yang, Q. Liang, Y. Xu, S. Fu, J. Yan, J. Zhou, J. Shi and M. Wu, *Chem. Eng. J.*, 2020, **390**, 124601.
27 C.-H. Huang and T.-M. Chen, *J. Phys. Chem. C*, 2011, **115**, 2349–2355.
28 Y. Yu, Q. Wu and R. Li, *J. Solid State Chem.*, 2006, **179**, 429–432.
29 W. Ullah Khan, S. B. Mane, S. Ullah Khan, D. Zhou, D. Khan, Q. Yu, W. Zhou, L. Zhou, J. Shi and M. Wu, *RSC Adv.*, 2018, **8**, 40693–40700.
30 W. U. Khan, W. U. Khan, H. Lin, Z. Cheng, M. W. Shah and Y. Zhang, *ACS Appl. Electron. Mater.*, 2021, **3**, 4218–4227.
31 N. U. Rahman, W. U. Khan, S. Khan, X. Chen, J. Khan, J. Zhao, Z. Yang, M. Wu and Z. Chi, *J. Mater. Chem. A*, 2019, **7**, 6467–6474.
32 Z. Xu, Z. Xia, B. Lei and Q. Liu, *J. Mater. Chem. C*, 2016, **4**, 9711–9716.
33 W. U. Khan, W. U. Khan, Y. Peng, Z. Cheng, T. A. Saleh and Y. Zhang, *J. Colloid Interface Sci.*, 2021, **600**, 219–228.
34 W. U. Khan, Z. Ye, M. Boubeche, T. Liu, Z. Guo and Y. Zhang, *J. Alloys Compd.*, 2021, **888**, 161538.
35 W. U. Khan, W. U. Khan, Z. Ye, M. Boubeche, T. Shi, D. Khan and Y. Zhang, *Ceram. Int.*, 2022, **48**, 5689–5697.
36 N. Yang, J. Li, Z. Zhang, D. Wen, Q. Liang, J. Zhou, J. Yan and J. Shi, *Chem. Mater.*, 2020, **32**, 6958–6967.

37 O. A. Lipina, L. L. Surat, Y. V. Baklanova, L. Y. Mironov, A. N. Enyashin, A. Y. Chufarov, A. P. Tyutyunnik and V. G. Zubkov, *New J. Chem.*, 2020, **44**, 16400–16411.
38 P. Du and J. S. Yu, *J. Alloys Compd.*, 2019, **785**, 789–797.
39 J. Li, Q. Liang, Y. Cao, J. Yan, J. Zhou, Y. Xu, L. Dolgov, Y. Meng, J. Shi and M. Wu, *ACS Appl. Mater. Interfaces*, 2018, **10**, 41479–41486.
40 G.-H. Li, N. Yang, J. Zhang, J.-Y. Si, Z.-L. Wang, G.-M. Cai and X.-J. Wang, *Inorg. Chem.*, 2020, **59**, 3894–3904.
41 P. Dang, G. Li, X. Yun, Q. Zhang, D. Liu, H. Lian, M. Shang and J. Lin, *Light: Sci. Appl.*, 2021, **10**, 1–13.
42 C. Guo, L. Luan, C. Chen, D. Huang and Q. Su, *Mater. Lett.*, 2008, **62**, 600–602.
43 Q. Zhang, X. Wang and Y. Wang, *Inorg. Chem. Front.*, 2020, **7**, 1034–1045.
44 J. Qiao, L. Ning, M. S. Molokeev, Y.-C. Chuang, Q. Liu and Z. Xia, *J. Am. Chem. Soc.*, 2018, **140**, 9730–9736.
45 M. Zhao, Z. Xia, X. Huang, L. Ning, R. Gautier, M. S. Molokeev, Y. Zhou, Y. C. Chuang, Q. Zhang, Q. Liu and K. R. Poeppelmeier, *Sci. Adv.*, 2019, **5**, eaav0363.
46 X. Zhang, Y.-T. Tsai, S.-M. Wu, Y.-C. Lin, J.-F. Lee, H.-S. Sheu, B.-M. Cheng and R.-S. Liu, *ACS Appl. Mater. Interfaces*, 2016, **8**, 19612–19617.
47 S. U. Khan, W. U. Khan, W. U. Khan, D. Khan, S. Saeed, S. Badshah, M. Ikram and T. A. Saleh, *Small*, 2020, **16**, 2001551.
48 D. Kang, H. S. Yoo, S. H. Jung, H. Kim and D. Y. Jeon, *J. Phys. Chem. C*, 2011, **115**, 24334–24340.
49 S. Bai, H. Liang, C. Li, C. Tang, G. Yang, X. Xu, X. Yang, G. Pan and Y. Zhu, *Ceram. Int.*, 2023, **49**, 1102–1107.
50 M. Liao, F. Wu, D. Zhu, X. Zhang, H. Dong, Z. Lin, M. Wen and Z. Mu, *Chem. Eng. J.*, 2022, **449**, 137801.
51 J. Chen, N. Zhang, C. Guo, F. Pan, X. Zhou, H. Suo, X. Zhao and E. M. Goldys, *ACS Appl. Mater. Interfaces*, 2016, **8**, 20856–20864.
52 C. Dzorkpata, S. Thapa, H. Zhu, A. Grigoriev, D. Babaian, S. Guha and P. Zhu, *J. Alloys Compd.*, 2024, **1005** 176064.
53 S. Thapa, G. C. Adhikari, H. Zhu, A. Grigoriev and P. Zhu, *Sci. Rep.*, 2019, **9**, 18636.
54 P. Zhu, S. Thapa, H. Zhu, S. Wheat, Y. Yue and D. Venugopal, *J. Alloys Compd.*, 2023, **960**, 170836.
55 Z. Yu, X. Li, J. Wang and S. Zhang, *Mater. Today Chem.*, 2023, **33**, 101739.
56 W. U. Khan, L. Zhou, X. Li, W. Zhou, D. Khan, S.-I. Niaz and M. Wu, *Chem. Eng. J.*, 2021, **410**, 128455.